Laser noise compression by filamentation at 400 nm in argon

Pierre Béjot*[(1)], Christophe Bonnet[(2)], Véronique Boutou[(2)], Jean-Pierre Wolf[(1)]

[(1)] *Université de Genève, GAP-Biophotonics, 20 rue de l'Ecole de Médecine, 1211 Geneva 4, Switzerland*

pierre.bejot@physics.unige.ch

[(2)] *Université Lyon 1, CNRS, LASIM UMR 5579, bt. A. Kastler, 43 Bvd du 11 novembre 1918, F-69622 Villeurbanne, France*

Abstract: Filamentation is an efficient way to produce an intense and spectrally broad, but poorly stable, source for coherent control spectroscopy. We first described both theoretically and experimentally the filamentation and broadening of a 410 nm ultrashort laser pulse in Argon. By observing the theoretical and experimental spectral cross-correlation in the filament, we then show that the stability of the source can be improved. The Signal-to-Noise Ratio of the intensity inside the filament is increased up to 7 dB by its spectral filtering which provide a low noise broad spectrum source.

OCIS codes: (190.3270) Kerr effect; (190.4380) Nonlinear optics, four-wave mixing; (320.7110) Ultrafast nonlinear optics; (030.6600) Statistical optics

References and links

1. T. Brixner, N. H. Damrauer, P. Niklaus, and G. Gerber, Photoselective adaptive femtosecond quantum control in the liquid phase, Nature **414**, 57–60 (2001).
2. J. M. Dela Cruz, I. Pastirk, V. V. Lozovoy, K. A. Walowicz, and M. Dantus, Multiphoton intrapulse interference 3: Probing microscopic chemical environments, J. Phys. Chem. A **108**, 53–58 (2004).
3. F. Courvoisier, V. Boutou, V. Wood, A. Bartelt, M. Roth, H. Rabitz, and J. P. Wolf, Femtosecond laser pulses distinguish bacteria from background urban aerosols, Appl. Phys. Lett. **87**, 063901 (2005).
4. V. V. Lozovoy and M. Dantus, Coherent control in femtochemistry, Chemphyschem **6**, 1970–2000 (2005).
5. A.M. Weiner, Femtosecond pulse shaping using spatial light modulators, Rev. Sci. Instrum. **71**, 1929–1960 (2000).
6. J. P. Ogilvie, D. Dbarre, X. Solinas, J. L. Martin, E. Beaurepaire and M. Joffre, Use of coherent control for selective two-photon fluorescence microscopy in live organisms, Opt. Express **14** (2), 759–766 (2006).
7. J. Kasparian, M. Rodriguez, G. Mejean, J. Yu, E. Salmon, H. Wille, R. Bourayou, S. Frey, Y. B. Andre, A. Mysyrowicz, R. Sauerbrey, J. P. Wolf, and L. Woste, White-light filaments for atmospheric analysis, Science **301**, 61–64 (2003).
8. H. Wille, M. Rodriguez, J. Kasparian, D. Mondelain, J. Yu, A. Mysyrowicz, R. Sauerbrey, J. P. Wolf, and L. Woste, Teramobile: A mobile femtosecond-terawatt laser and detection system, Eur. Phys. J: Appl. Phys. **20**, 183–190 (2002).
9. S. Coudreau, D. Kaplan, and P. Tournois, Ultraviolet acousto-optic programmable dispersive filter laser pulse shaping in KDP, Opt. Lett. **12**, 1899–1901 (2006).
10. M. Hacker, G. Stobrawa, R. Sauerbrey, T. Buckup, M. Motzkus, M. Wildenhain, and A. Gehner, Micromirror SLM for femtosecond pulse shapiing in the ultraviolet, Appl. Phys. B, **76**, 711–714 (2003).
11. F. G. Omenetto, B. P. Luce, and A. J. Taylor, Genetic algorithm pulse shaping for optimum femtosecond propagation in optical fibers, J. Opt. Soc. Am. B, **16**, 2005–2009 (1999).
12. Z. Cheng, G. Tempea, T. Brabec, K. Ferencz, C. Spielman, and F. Krausz, Generation of Intense Diffraction-Limited White Light and 4-fs Pulses, *Lasers and Electro-Optics Europe, 1998. 1998 CLEO/Europe. Conference on*

#85217 - $15.00 USD Received 17 Jul 2007; revised 23 Aug 2007; accepted 29 Aug 2007; published 28 Sep 2007

13. C. P. Hauri, W. Kornelis, F. W. Helbing, A. Heinrich, A. Couairon, A. Mysyrowicz, J. Biegert, and U. Keller, Generation of intense, carrier-envelope phase-locked few-cycle laser pulses through filamentation, Appl. Phys. B **79**, 673–677 (2004)
14. A. Couairon and A. Mysyrowicz, Femtosecond filamentation in transparent media, Phys. Rep. **441**, 47–189 (2007).
15. G. Mejean, J. Kasparian, J. Yu, S. Frey, E. Salmon, R. Ackermann, J. P. Wolf, L. Berge, and S. Skupin, Uv-supercontinuum generated by femtosecond pulse filamentation in air: Meter-range experiments versus numerical simulations, Appl. Phys. B, **82**, 341–345 (2006).
16. S. L. Chin, F. Thberge, W. Liu, Filamentation nonlinear optics, Appl. Phys. B **86**, 477–483 (2007).
17. S. R. Friberg, S. Machida, M. J. Werner, A. Levanon, and T. Mukai, Observation of optical soliton photon-number squeezing, Phys. Rev. Lett. **77**, 3775–3778 (1996).
18. S. Spalter, N. Korolkova, F. Konig, A. Sizmann, and G. Leuchs, Observation of multimode quantum correlations in fiber optical solitons, Phys. Rev. Lett. **81**, 786–789 (1998).
19. L. Boivin, F. X. Kartner, and H. A. Haus, Analytical solution to the quantum-field theory of self-phase modulation with a finite response-time, Phys. Rev. Lett. **73**, 240–243 (1994).
20. T. Opatrny, N. Korolkova, and G. Leuchs, Mode structure and photon number correlations in squeezed quantum pulses, Phys. Rev. A **66**, 053813 (2002).
21. E. Schmidt, L. Knoll, and D. G. Welsch, Cumulant expansion for studying damped quantum solitons, Phys. Rev. A **59**, 2442–2457 (1999).
22. M. Mlejnek, E. M. Wright, and J. V. Moloney, Femtosecond pulse propagation in argon: A pressure dependence study, Phys. Rev. E **58**, 4903–4910 (1998).
23. H. Ehrhardt, Hesselba.Kh, K. Jung, E. Schubert, and K. Willmann, Electron-impact ionization of argon - measurements of triple differential cross-sections, J. Phys. B **7**, 69–78 (1974).
24. M. D. Feit and J. A. Fleck, Effect of refraction on spot-size dependence of laser-induced breakdown, Appl. Phys. Lett. **24**, 169–172 (1974).
25. A. Couairon, S. Tzortzakis, L. Berge, M. Franco, B. Prade, and A. Mysyrowicz, Infrared femtosecond light filaments in air: simulations and experiments, J. Opt. Soc. Am. B **19**, 1117–1131 (2002).
26. W. H. Press, B. P. Flannery, S. A. Teukolsky, and W. T. Vetterling, Numerical recipies, *Cambridge University Press, Cambridge*, Numerical Recipies, 1989.
27. A. Chiron, B. Lamouroux, R. Lange, J. F. Ripoche, M. Franco, B. Prade, G. Bonnaud, G. Riazuelo, and A. Mysyrowicz, Numerical simulations of the nonlinear propagation of femtosecond optical pulses in gases, Eur. Phys. J D **6**, 383–396 (1999).
28. E. R. Peck and D. J. Fischer, Dispersion of argon, J. Opt. Soc. Am. **54**, 1362–1364 (1964).
29. V. Mizrahi and D. P. Shelton, Dispersion of nonlinear susceptibilities of Ar, N_2, and O_2 measured and compared, Phys. Rev. Lett. **55**, 696–699 (1985).
30. Y. P. Raizer, Plasma physics, *Springer, Berlin*, Plasma Physics (1994).
31. A. Couairon and L. Berge, Light filaments in air for ultraviolet and infrared wavelengths, Phys. Rev. Lett. **88**, 135003 (2002).
32. S. Champeaux and L. Berge, Femtosecond pulse compression in pressure-gas cells filled with argon, Phys. Rev. E **68**, 066603 (2003).
33. T. Brixner, N. H. Damrauer, B. Kiefer, and G. Gerber, Liquid-phase adaptive femtosecond quantum control: Removing intrinsic intensity dependencies, J. Chem. Phys. **118**, 3692–3701 (2003).
34. P. Bejot, J. Kasparian, E. Salmon, R. Ackermann, N. Gisin, and J. P. Wolf, Laser noise reduction in air, Appl. Phys. Lett. **88**, 251112 (2006).
35. P. Bejot, J. Kasparian, E. Salmon, R. Ackermann, and J. P. Wolf, Spectral correlation and noise reduction in laser filaments, Appl. Phys. B **87**, 1–4 (2007).

1. Introduction

Increasing interest has been recently devoted to selective excitation of biological samples [1, 2, 3] by means of pump-pump spectroscopy or more sophisticated coherent control schemes. These experiments require to shape broadband low noise coherent source which until recently was only feasible in the near infrared whereas the absorption bands of most of the relevant optically active biological molecules (tryptophan, flavin, heme molecules,...) are located in the UV-Visible region. Therefore, previous coherent control experiments in this field usually involved two-photon excited fluorescence [4, 5] induced by shaped intense ultrashort 800 nm laser pulses for instance to selectively excite the fluorescence in live organisms [6]. However, due to their inherently weak cross-section and nonlinear nature, two-photon based experiments need a tightly focused laser which could turn out to be critical to implement for long-distance applications,

#85217 - $15.00 USD Received 17 Jul 2007; revised 23 Aug 2007; accepted 29 Aug 2007; published 28 Sep 2007

even if recent advances in ultrafast lasers have shown that high-power laser light such as the Teramobile [7, 8] can, under certain power and focusing conditions, create extended regions of ultra-intense illumination. Recently, considerable interest has been dedicated to the realization of UV-Visible pulse shapers [9, 10], opening the way for remote excited fluorescence with shaped laser pulse around 400 nm which is an interesting spectral window for biomolecules. To achieve this goal, an intense and stable source, with a spectrum sufficiently broad to overlap a manifold of transition pathways of the target molecule, is highly desirable. The stability is an issue in particular for applications relying on closed-loop optimization schemes, the most popular being those based on genetic algorithms [11].

An easy and efficient way to provide broad spectrum femtosecond laser pulses is to use filamentation. [13] Filaments [14] arise in the nonlinear propagation of ultrashort, high-power laser pulses in transparent media. They result from a dynamic balance between Kerr-self-focusing and defocusing by self-induced plasma. These spatio-temporal solitonic structures are able to generate an extraordinary broad supercontinuum by self-phase modulation (SPM) and four wave mixing (FWM), spanning from the UV to the IR [15]. Filamentation around 400 nm in a controlled medium such as Argon under several bar could then be a promising way to produce an intense broad spectrum for pulse shaping applications. Even if recent works [16] show that the overall intensity inside the filament core is stabilized, considering the inherent high order nonlinear nature of the filamentation process, the filament spectrum is very sensitive to the noise of the input beam, which could be a critical drawback for using filaments in connection to closed-loop optimization. Moreover, theoretical and experimental investigations in optical fibers showed that spectral correlations and photon number squeezing occur in temporal solitons [17, 18]. Correlations within the white light continuum is due to SPM and FWM [19] processes, where the medium participates only as the mediator of the nonlinear mixing. Under these circumstances, two photons at ω_0 are converted into a pair of photons at the conjugated wavelengths ω_1 and ω_2 such that the energy is still conserved $(2\omega_0 = \omega_1 + \omega_2)$. This process results in typical correlation maps, where the signal at wavelengths within the continuum appears anticorrelated with the incident one, while pairs of conjugated wavelengths are strongly correlated. Such maps are very well reproduced by numerical simulations [20, 21]. The authors also showed that the correlation maps may feature more complex patterns, due to cascaded FWM events in which photons originating from a first χ^3 process give rise to further FWM, so that correlations are partly lost. This occurs for longer propagation distances, higher pulse energies, or larger χ^3 values.

To our knowledge, no theoretical model is available for filamentation at 400 nm. For that purpose, we developed a theoretical model based on the derivation of a numerical solution of the time-dependent non linear Schrodinger equation to study the feasibility of inducing such a source.

In this paper, we demonstrate that spectral intensity correlations occur in the UV-Visible supercontinuum generated by filamentation of a 400 nm ultrashort pulse in Argon. We also make use of these correlations experimentally to compress the laser noise, by spectral filtering of the broadened output. A laser noise reduction as high as 7 dB is demonstrated with this method. Our study shows, therefore, that filamentation can produce a source which fulfils the conditions for pulse shaping applications.

#85217 - $15.00 USD Received 17 Jul 2007; revised 23 Aug 2007; accepted 29 Aug 2007; published 28 Sep 2007

2. Theoretical background

2.1. Basic equations

We consider a linearly polarized incident electric field at $\lambda_0 = 410\ nm$ with cylindrical symmetry around the propagation axis z, written as $\Re e\{\varepsilon \exp[i(k_0 z - \omega_0 t)]\}$, where $k_0 = \frac{2\pi n_0}{\lambda_0}$ and $\omega_0 = \frac{2\pi c}{\lambda_0}$ are the wave number and the frequency of the carrier wave respectively. The scalar envelope $\varepsilon(r,t,z)$ is assumed to be slowly varying in time and along z and evolves according to the propagation equation derive in [22].

$$\partial_z \varepsilon = \frac{i}{2k_0}\triangle_\perp^2 \varepsilon - i\frac{k''}{2}\partial_t^2 \varepsilon + \frac{ik_0 n_2}{n_0}|\varepsilon|^2\varepsilon - \frac{ik_0}{2n_0^2\rho_c}\rho\varepsilon - \frac{1}{2}\sigma\rho\varepsilon - \frac{\beta^K}{2}|\varepsilon|^{2K-2}\varepsilon \tag{1}$$

where t refers to the retarded time in the reference frame of the pulse $t \rightarrow t - \frac{z}{v_g}$ with $v_g = \frac{\partial\omega}{\partial k}|_{\omega_0}$ corresponding to the group velocity of the carrier envelope. The terms on the right-hand side of Eq. 1 account for spatial diffraction, second order dispersion, instantaneous Kerr effect, plasma absorption and defocusing, respectively. The Kerr response of Argon is assumed to be instantaneous [14]. In (1), $\rho_c = \frac{\omega_0 m_e \varepsilon_0}{q_e^2}$ corresponds to the critical plasma density above which the plasma becomes opaque. In addition, the constant $\sigma = \frac{ke^2}{\omega m \varepsilon_0}\frac{\tau}{1+(\omega\tau)^2}$ denotes the cross-section for electron-neutral inverse bremsstrahlung (τ is the electron-atom relaxation time) and β^K corresponds to the coefficient of multiphoton absorption, K being the minimal number of photons necessary to ionize Argon. This quantity is calculated as $K = mod(\frac{U_i}{\hbar\omega_0}) + 1$, where U_i is the ionization potential of Argon ($U_i = 15.76\ eV$ [23]). β^K is expressed as $\beta^K = K\hbar\omega_0\rho_{at}\sigma_K$ where ρ_{at} is the Argon density and σ_K is the multiphoton ionization cross section. The dynamic of the electric field is coupled with the plasma density ρ because of the multiphoton ionization process. The ionization of Argon follows the equation [24]:

$$\partial_t \rho = \sigma_K(1 - \frac{\rho}{\rho_{at}}|\varepsilon|^{2K}) + \frac{\sigma}{U_i}\rho|\varepsilon|^2 - \alpha\rho^2 \tag{2}$$

We chose an initial plasma density of $10^9 e^-.cm^{-3}$. [25] The input electric field envelope is modeled in focused geometry by a Gaussian profile with input power P_{in} as

$$\varepsilon(r,t,0) = \sqrt{\frac{2P_{in}}{\pi w_0^2} exp(-\frac{r^2}{w_0^2} - (1+iC)\frac{t^2}{\tau_p^2} + i\frac{k_0 r^2}{2f})} \tag{3}$$

Our numerical method is based on a Fourier Split-Step scheme in which all the linear terms are computed in the Fourier space over a half-step while the nonlinear terms are directly computed in the physical space over a second half-step using a Runge-Kutta procedure. To integrate the linear terms of the equation along the z axis, i.e. the diffraction and dispersion, we used a Crank-Nicholson scheme [26], more stable than the Euler method [27]. On the other hand, for the plasma Eq. (2), an Euler scheme is sufficiently robust.

For calculation time concerns, the meshgrid size, as well as the integration step, varied during the simulation. More precisely, we used a (1400 ; 2048) meshgrid to describe the pulses. The size of the meshgrid was chosen in the first part of the calculation, to be ($5w_0$; 10Δt). As soon as the quadratic radius of the pulse is divided by a factor 2, the resolution of the meshgrid is increased by a factor 2. So, in the first part of the calculation, the radial resolution is only $\frac{5w_0}{1400}$=21 μm, then it becomes 10.5 μm and finally increases to 5.3 μm which is sufficient for

#85217 - $15.00 USD Received 17 Jul 2007; revised 23 Aug 2007; accepted 29 Aug 2007; published 28 Sep 2007

resolving the plasma channel. In order to increase the resolution of the meshgrid, we used a cubic spline interpolation of the electric field (sampling error $< 0.1\%$ over the entire meshgrid). At the beginning of the propagation, a low resolution is sufficient because none of the nonlinear terms does not play a significant role in the propagation. Then the Kerr effect induces a plasma channel. As soon as plasma ionization becomes significant, the meshgrid has to resolve the plasma channel which has a FWHM width of a few microns. Hence the meshgrid resolution turns out to be relevant for any propagation step. This latter also changed during the propagation. It is initially fixed at 2 mm. Then because the nonlinear phase varies as $|\varepsilon|^2 dz$, we control the relative error by decreasing the propagation step as a function of $\frac{1}{max(|\varepsilon|^2)}$ and this, down to 10 μm during the filamentation process.

λ_0 (nm)	410
k'' ($fs^2.cm^{-1}$) [28]	$0.39p$
n_2 (m^2W^{-1}) [29]	$4.9.p\ 10^{-23}$
K	6
β^K ($m^{2K-3}W^{1-K}$)	$1.95.p\ 10^{-88}$
σ^K ($s^{-1}cm^{2K}W^{-K}$) [14]	$2.79.p\ 10^{-72}$
$\sigma(1bar)$ (m^2)	$2.65\ 10^{-24}$
ρ_c (m^{-3})	$6.64\ 10^{27}$
α ($m^{-3}s^{-1}$) [22]	$7\ 10^{-13}$
τ (s) [30]	$1.9\ 10^{-13}p^{-1}$

Table 1. Physical parameters used in the model (p accounts for the relative gas pressure: $p = \frac{P}{1bar}$).

2.2. Results and discussion

For the numerical simulations presented below, we chose the parameters to be consistent with our experiments. We considered the propagation of $\lambda_0 = 410\ nm$ Fourier Transformed limited Gaussian laser pulses with a pulse duration $\Delta t = \sqrt{2log(2)}\tau_p = 150\ fs$ (FHWM). The critical power was calculated using $P_{cr} = \frac{\lambda_0^2}{2\pi n_0 n_2} = 0.54\ GW$. In the experiments, the laser system provided a laser energy up to 1 mJ. In simulations, however, we fixed the laser energy to a value of 135 μJ which corresponds to about 5 P_{cr} at a pressure of 5 bar, which is the pressure used in the calculations below. We chose an input beam with an intensity FWHM diameter of 6 *mm* and a focal length of 75 *cm*. Table I summarizes all the physical parameter values we used in our model. Some parameters are given as a function of p which is the relative gas pressure.

In Fig.1, the temporal and spatial dependencies of the electric field intensity are displayed for several distances ($z = 0\ m, z = 75\ cm, z = 78\ cm, z = 80\ cm, z = 84\ cm$ and $z = 99\ cm$). The vertical axis represents the radial distance (in μm), whereas the horizontal axis represents the retarded time (in fs). When the intensity peak reaches a value of about $6\ 10^{13}\ W.cm^{-2}$, the plasma contribution becomes higher than that of the Kerr effect for the trailing edge because the ionization threshold is reached. Therefore the trailing edge is defocused (see $z = 80\ cm$). The plasma density subsequently decreases so that the trailing part of the pulse focuses again when the power is high enough (see $z = 84\ cm$). In such a case, the pulse is divided into two subpulses (Fig. 2(a)). For even longer propagation distance, the mechanism is rather complex because it involves pulse splitting and self-phase modulation modified by ionization. Consequently, the resulting electric field intensity is divided in several subpulses (Fig. 1, $z = 99\ cm$).

#85217 - $15.00 USD Received 17 Jul 2007; revised 23 Aug 2007; accepted 29 Aug 2007; published 28 Sep 2007

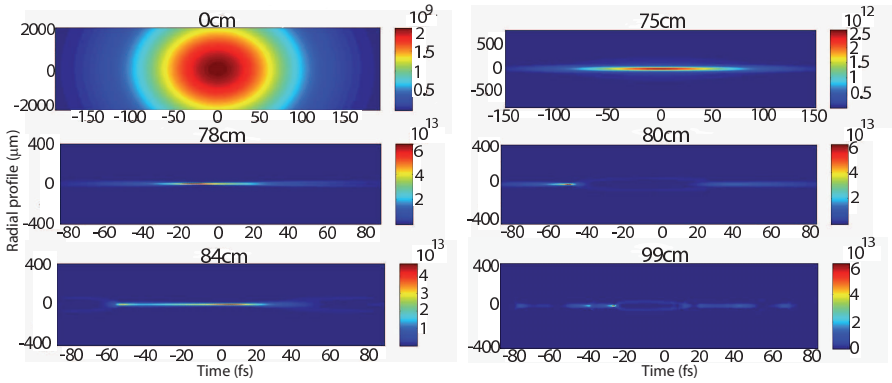

Fig. 1. Time-Space representation of the electric field intensity focused by a 75 cm focal lens. The initial energy was set at 135 μJ and the duration at 150 fs. The Argon cell pressure was 5*bar*. It has been plotted for several distances which are relevant in the filamentation process. The beam is first focused and when the intensity reaches about 6.5 10^{13} $W.cm^{-2}$, the plasma defocuses the trailing part of the pulse (78 cm). If the energy is sufficient, the trailing part focuses again, forming a subpulse (80 cm). In the last part of the filamentation process, several subpulses was created (99 cm).

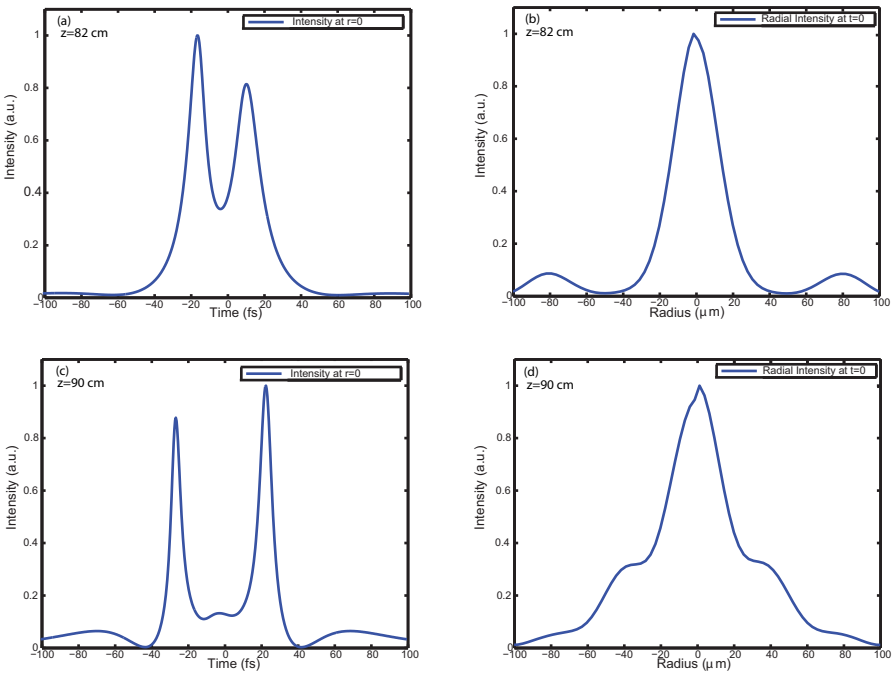

Fig. 2. Left: Time-dependent intensity at the center the pulse for z=82 cm and z=90 cm. At the beginning of the filamentation process (a), the pulse is divided into two subpulses. Then (c), several subpulses are formed. Right: Radial-dependent intensity of the pulse for z=82 cm and z=90 cm. The FWHM radius is about 80 μm

#85217 - $15.00 USD Received 17 Jul 2007; revised 23 Aug 2007; accepted 29 Aug 2007; published 28 Sep 2007

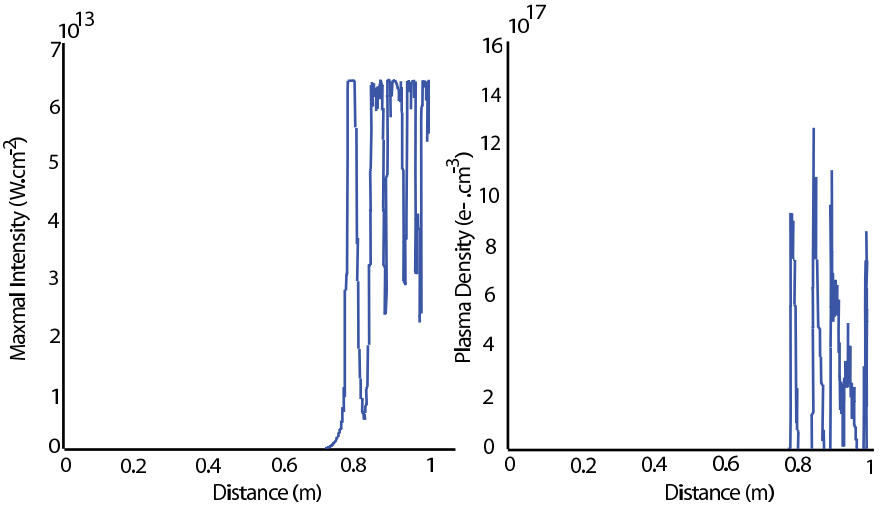

Fig. 3. Left: Maximal intensity inside the core of the filament ($W.cm^{-2}$). The Argon cell pressure was 5 bar. The inside filament core intensity is clamped at about 6.5 10^{13} $W.cm^{-2}$. Right: Maximal plasma density inside the filament (e^- cm^{-3}). The oscillations observed are inherent to the non linear propagation: as soon as the plasma density reaches its maximum, the filament intensity decreases because the plasma defocuses the beam.

Filamentation is also illustrated in Fig. 3, where we have plotted both the maximum intensity and the maximum plasma density reached for each propagation step. The maximal intensity is clamped and reaches a value of about 6.5 10^{13} $W.cm^{-2}$ because the generated electron density has a threshold like response, which saturates self-focusing locally and limits the peak intensity inside the filament by defocusing the beam. Concerning the plasma density, it reaches a value of about 10^{17-18} $e^- cm^{-3}$. This value is consistent with previous calculations with other wavelengths in Argon or in the air (248 nm, 586 nm and 810 nm) [31, 32]. The maximum electron density crucially depends on the initial curvature radius of the beam. In particular, the more the beam is focused, the higher the plasma density, as observed experimentally.

Figure 4 shows the evolution of the radius of the beam as a function of the propagation distance. In the spatial domain, the filament core diameter FWHM is about 80 μm (see Fig. 3, Right, inset) but this calculation does not take into account the photon bath which feeds the filament core. Therefore, it is preferable to consider the quadratic radius calculated as

$$R_{quad} = \sqrt{\frac{\int r^2 (\int |\varepsilon(r,t)|^2 dt) dr}{\int \int |\varepsilon(r,t)|^2 dt dr}} \tag{4}$$

In that case, as shown on Fig. 3, (left side), the beam radius at the end of the propagation is close to 300 μm.

Figure 5(a) represents theoretical spectra for several Argon pressures. Both the broadness and the shape can be controlled by adjusting the Argon pressure and the initial chirp. These two parameters are simple to set and allow a relatively good control of the spectrum. As illustrated in Fig. 5(b), calculated spectra are in relatively good agreement with experimental ones which validates the use of our model for further observations of correlations.

#85217 - $15.00 USD Received 17 Jul 2007; revised 23 Aug 2007; accepted 29 Aug 2007; published 28 Sep 2007

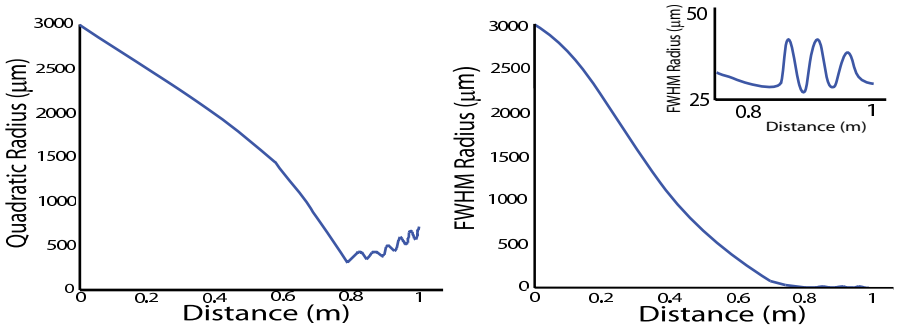

Fig. 4. Left: quadratic radius calculated as (Eq.3). This radius takes into account the filament bath which increases the total quadratic radius ($\simeq 300\ \mu m$). Right: FWHM radius: The filament core diameter is about 80 μm.

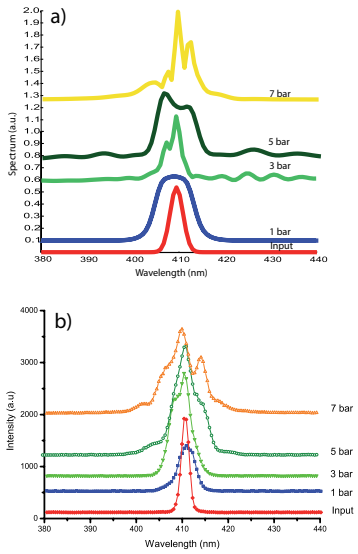

Fig. 5. (a) Theoretical spectra of the filament after propagation in Argon for different pressures. The shape and broadness of the spectrum can therefore be controlled by adjusting the pressure. (b)Experimental spectra broadened by self-phase modulation for various argon pressures. The energy was set at 150 μJ. The higher is the pressure, the broader would be the spectrum. At relatively high pressure, oscillations also appear in spectra, in good agreement with calculations.

#85217 - $15.00 USD Received 17 Jul 2007; revised 23 Aug 2007; accepted 29 Sep 2007

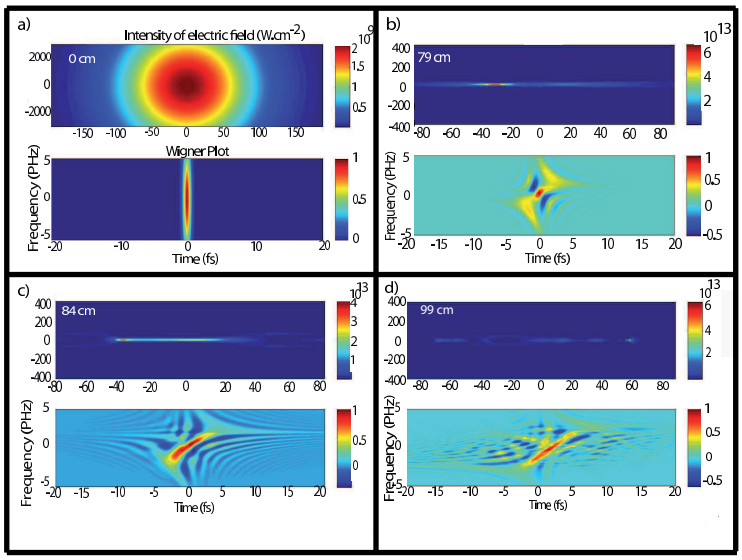

Fig. 6. In each square: up, the spatio-temporal dependencies of the intensity for several distances, down, the corresponding Wigner plot of the pulse. At the end of the filamentation process, the electric field is chirped by 2 fs^2 .

We then further calculated the Wigner function [33] of the electric field for each propagation step as

$$W(t,\omega) = \int E(\omega + \frac{\Omega}{2}) E^*(\omega - \frac{\Omega}{2}) e^{-i\Omega t} d\Omega \tag{5}$$

The Wigner plot allows a better understanding of the time-frequency properties of the propagation. For instance, the chirp generated during the filamentation process is clearly visible in such a representation. In the first part of the filamentation process, one can model the phase of the electric field as:

$$\Phi(t) = k_0 z - \omega_0 t = (\frac{n}{c} z - t)\omega_0 = ((n_0 + n_2 I(t) - \frac{\rho}{2n_0\rho_c})\frac{z}{c} - t)\omega_0 \tag{6}$$

and so the instantaneous frequency, can be written as

$$\omega(t) = -\partial_t \Phi = (-n_2 \partial_t I + \frac{1}{2n_0\rho_c}\partial_t \rho + 1)\omega_0 \frac{z}{c} \tag{7}$$

That means that, at the beginning of the filamentation process, when only SPM plays a significant role, the upper frequencies are created in the trailing edge of the pulse whereas the lower frequencies are created in its leading part. SPM induces therefore a temporal chirp in the pulse. Moreover the plasma generation tends to generate higher frequencies when the time gradient of the plasma density becomes significant. Hence, in Fig. 6, although the initial pulse is not chirped, at the end of the filamentation, a chirp of 2 fs^2 is observed on the electric field.

As a conclusion, filamentation at 400 nm turns out to be a good candidate to obtain a source for UV shaping applications. The filamentation dynamic is quite similar to these of the 800 nm filamentation (similar intensity, plasma density). However, because the 400 nm photons are

#85217 - $15.00 USD Received 17 Jul 2007; revised 23 Aug 2007; accepted 29 Aug 2007; published 28 Sep 2007

more energetic than these at 800 nm, the order of the plasma nonlinearity is higher at 800 nm (5 photons at 400nm against 8 photons at 800 nm are necessary to ionize Argon). Moreover all the constants underlying the filamentation process are different: GVD, ionization cross-section, absorption,... So, even if there are a lot of similarities in the dynamic, the spatiotemporal properties of the two filaments are different: the filament at 400 nm is smaller (typically 80 μm instead of 100 μm at 800 nm) but it implies a less efficient white-light generation. However, 400 nm filament generates a sufficiently broad spectrum and its shape can be tailored with simple parameters such as chirp and gas pressure. Moreover, the filament is intrinsically energetic which is favorable for remote sensing applications. However, the filamentation process is highly nonlinear, which means that small changes in the input beam induce strong variations of the filament spectrum. This instability is the main drawback of using filament as a usefull coherent source for closed-loop optimization experiments. However, the statistical properties of filamentation can be used to restrict, up to a certain point, this instability. Recent studies [34, 35] indeed show that correlations exist between specific wavelengths pairs. These correlations are positive if the wavelengths are created simultaneously, negative if one wavelength is used to create the other. The variance of the intensity $\sigma^2(I) = < I^2 > - < I >^2$ (where $< X >$ denotes the average of X over a representative sample) can be written as

$$\sigma^2(I) = \int\int cov(I(\lambda_1), I(\lambda_2)) d\lambda_1 d\lambda_2 \tag{8}$$

So if with a specific spectral filter, one can select anticorrelated wavelengths and reject correlated wavelengths, then the signal-to-noise ratio can be significantly increased. One way to observe correlations is to calculate the propagation cross-correlation for each wavelengths couple as

$$C_{th}(\lambda_1, \lambda_2) = \frac{Cov(I(\lambda_1), I(\lambda_2))}{\sqrt{Cov(I(\lambda_1), I(\lambda_1)) Cov(I(\lambda_2), I(\lambda_2))}} \tag{9}$$

where

$$Cov(I(\lambda_1), I(\lambda_2)) = E([I(\lambda_1, z) - \bar{I}(\lambda_1)][I(\lambda_2, z) - \bar{I}(\lambda_2)]) \tag{10}$$

, E being the mathematical expectation and $I(\bar{\lambda_i})$ the average of $I(\lambda_i, z)$ over the propagation calculated as:

$$\bar{I}(\lambda_i) = \frac{\int_0^{L_{tot}} I(\lambda_i, z) dz}{L_{tot}} \tag{11}$$

To observe experimentally this quantity would require to take spectra at many propagation distances for an unique shot, which is fastidious. However, even if this quantity is not measurable experimentally, it indicates in what manner the spectrum is broadened during the filament propagation. The correlation maps resulting from Eq. 9, plotted in Fig. 7. for two different pressures, display two typical patterns. At low pressure, both left- and right-hand sides of the spectrum, which correspond to wavelengths induced during the propagation, are correlated. A maximum is reached for perfectly conjugated wavelengths which satisfy $2\omega_0 = \omega_1 + \omega_2$ (these wavelengths pairs are indicated by the white solid line on the map of Fig. 7). In contrast, the pump frequency ω_0 is anticorrelated with the two sides of the spectrum. These properties suggest that, in the low pressure regime, the preponderant phenomenon is the χ^3 process $2\omega_0 = \omega_1 + \omega_2$. Above 3-4 critical power, i.e. at higher pressure (for example p=5 bars in Fig. 7), oscillations appear in the correlation map which means that to generate outer wavelengths, previously induced photons are used in cascading processes.

#85217 - $15.00 USD Received 17 Jul 2007; revised 23 Aug 2007; accepted 29 Aug 2007; published 28 Sep 2007

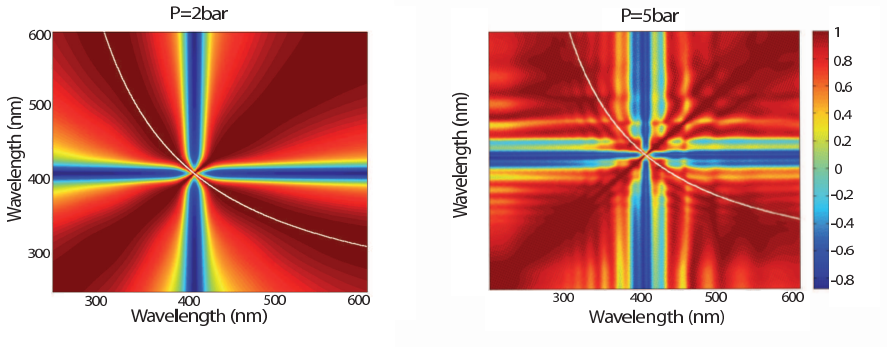

Fig. 7. Correlation map for two different pressures. Solid line corresponds to couples of wavelengths (ω_1, ω_2) which satisfy $2\omega_0 = \omega_1 + \omega_2$ (6). Left: in the low pressure regime ($P = 2$ *bar*), the highest correlation is reached for wavelengths couples which satisfy (6). Right: in the higher pressure regime ($P = 5$ *bar*), oscillations appear in the correlation map which is a characteristic of cascading processes. The highest correlations do not correspond anymore to wavelengths couples which satisfy (6): initial correlations are partly lost.

3. Experiments

3.1. Experimental setup

A CPA (Chirped Pulse Amplification) Ti: Sapphire laser system delivered 150 fs pulses at 22.5 Hz repetition rate, centered at 810 nm, with $\simeq$ 6 mm beam diameter (at e^{-2} level). A 1 mm BBO crystal was used for frequency doubling the fundamental wavelength. Adequate filters and dichroic mirrors allow to reject the residual of the fundamental. The beam energy at 410 nm could be varied up to 1 mJ. As depicted in Fig. 8, the 410 nm beam was focused by a 75 cm lens inside a 1m length cell containing Argon. The Argon pressure was varied from 1 to 8 bar. Depending on the pressure, the filament formed about the center of the cell was typically a few centimeters long. At the cell exit, as shown in Fig. 8(a), after about 50 cm of free propagation outside the Argon cell, the beam was scattered on a neutral target, and the light was collected with a fiber and injected into a spectrometer (Ocean Optics HR2000) providing 0.6 nm resolution between 380 and 450 nm. 1000 spectra were recorded and used to compute the intensity cross-correlation maps across the spectrum. The cross-correlation between two wavelengths λ_1 and λ_2 was calculated as

$$C_{exp}(\lambda_1, \lambda_2) = \frac{V(n_1+n_2) - (V(n_1)+V(n_2))}{2\sqrt{V(n_1)V(n_2)}} \tag{12}$$

, with $V(x)$ the variance of variable x and n_i the photon number (or the intensity) at the wavelength λ_i. Hence, the cross-correlation measured experimentally (whereas it was not the case theoretically) is a statistical property of the filamentation. In a second experimental arrangement, depicted on Fig. 8(b), the continuum generated by the filament in argon was further dispersed by a diffraction grating (order -1 blazed, efficiency 75 % at 410 nm). The setup was used to observe the noise reduction induced by self phase modulation on the central wavelength. For that purpose, after the dispersion of the beam on the grating, an iris was placed in the Fourier plane of two cylindrical lenses in order to filter out the edge frequencies of the continuum. The remaining part of the beam was then detected on a photomultiplier tube (PMT) connected to a boxcar amplifier. Another PMT, located before the argon filled cell, was dedicated to measure simultaneously the laser input fluctuations. Acquisitions of about 2000 laser shots have

#85217 - $15.00 USD Received 17 Jul 2007; revised 23 Aug 2007; accepted 29 Aug 2007; published 28 Sep 2007

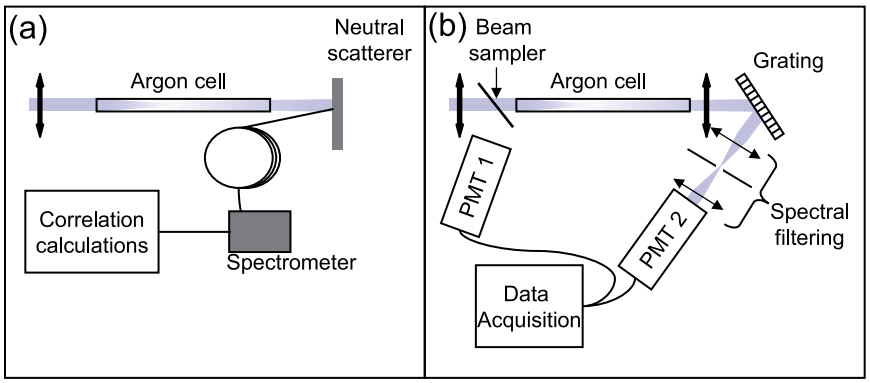

Fig. 8. (a). Correlation measurements setup up: the second harmonic of a Ti:Sa laser pulse (at 410 nm) is focused in a cell filled with argon. During its self-channeled propagation in the cell, its spectrum is broadened by self phase modulation. The scattering of broadened pulses on a neutral target is collected on a spectrometer via an optical fiber. Cross-correlations $C(\lambda_1, \lambda_2)$ are then calculated for several argon pressure to retrieve correlations maps. (b) Noise reduction setup: in that case, after their propagation, laser pulses are dispersed onto a grating before entering a spectral filtering setup composed of an adjustable iris in the Fourier plane of two cylindrical lenses. The filtered broaden spectrum (collected on PMT2) is then compared to a sample of the input spectrum (PMT1) in order to observe noise reduction as a function of the argon pressure in the cell.

been performed for each pressure and/or each position and size of the iris in order to retrieve histograms of the signal prior and after nonlinear propagation in the argon filled cell. Optimal parameters maximizing the Signal-to-Noise Ratio were determined from these histograms.

3.2. Results and discussions

Figure 5(b) shows the broadened spectrum as a function of the argon pressure in the cell. As described by Mlejnek et al. [22], the pulse propagation in the 1-8 bar domain results from equilibrium between self-focusing and plasma effects and can lead to stable propagation. Typically, the nearly Gaussian input spectrum (FWHM = 3 nm) is broadened by Kerr induced self phase modulation, while propagating through the cell. At 1 bar, the critical power, $P_{cr} = \frac{\lambda_0^2}{2\pi n_0 n_2}$ is about 0.5 GW in argon around $\lambda_0 = 410$ *nm*. At higher pressures, the critical power decreases and therefore lowers the threshold, yielding to a larger broadening of the input pulses. As expected from χ^3 induced broadening processes, two photons from the pump at λ_0 are annihilated to produce one photon at λ_1 and its conjugated photon at λ_2 (through the conservation of the energy, $\frac{2}{\lambda_0} = \frac{1}{\lambda_1} + \frac{1}{\lambda_2}$) , which produces correlations in the spectrum. The occurrence of correlations essentially depends of the physical parameters involved in the propagation (input energy, argon pressure). Figure 9 shows cross-correlation maps of the white-light continuum retrieved from typically 1000 spectra for several argon pressures and before propagation through the cell. In this latter case (”Reference” in Fig. 9), only positive correlations are observed. This is the signature of overall intensity fluctuations on the incident laser pulses. It indicates that fluctuations on the intensity of each wavelength are coherent. For propagation at low pressure (i.e. 2 bar), positive intensity correlations are observed in regions corresponding to nearly conjugated wavelength as well as in the trivial case $\lambda_1 = \lambda_2$, whereas negative correlations form a

#85217 - $15.00 USD Received 17 Jul 2007; revised 23 Aug 2007; accepted 29 Aug 2007; published 28 Sep 2007

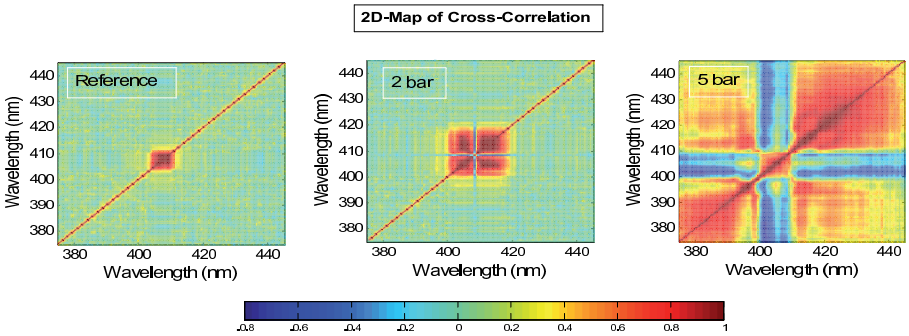

Fig. 9. Experimental cross-correlation maps as a function of argon pressure for an input pulse energy of 275 μJ. Before propagation (Reference), only positive correlations are observed for fundamental wavelengths (consistent with initial overall coherent fluctuations on the incident intensity). After propagation, for low pressure (2 bar), additional positive correlations are observed for conjugated wavelengths (pairs of photons) whereas negative correlations appear between these wavelengths and input wavelengths annihilated in the χ^3 process. At even higher pressure (5 bar), cascading events occur (visible through additional strips) which blur the reading of cross-correlation maps.

dark cross centered on λ_0. Up to 3 bar, the increase of the positive correlations area reflects further broadening of the input pulse and the creation of conjugated wavelengths. At higher pressure (for example, 5 bar on Fig. 9), cascaded events are responsible for the occurrence of new negative correlations (additional dark stripes). As described previously in the calculations section, when the spectrum is broadened enough, one or both conjugated wavelengths can be involved in a secondary event involving the third order polarization, which partially destroy the previously formed correlations.

The appearance of negative correlations also highlights the fact that a reduction of the noise on the intensity of the input spectrum is measurable. In order to observe fluctuations on the noise intensity, spectral filtering has been realized as described in the experimental section Fig. 10 shows histograms of the signal intensity before (S_1) and after (S_2) (with spectral filtering [406-414 nm]) propagation through the cell (argon pressure 2 bar). As compared to the incoming beam, filamentation yields a SNR increase of about 7 dB. This noise reduction disappears if spectral filtering is applied only to one side of the spectrum as SPM rejects the fluctuations to the two edges of the spectrum.

Noise compression can also be visualized by plotting the intensities of the spectrally filtered continuum (S_2) versus the intensities on the channel before filamentation (S_1). In Fig. 11, such plots are given as a function of the gas pressure inside the cell. For pressure lower than 2.5 bar, S_2 is an affine function of S_1 ($S_2 \simeq 0.9S_1$). The broadening does not take place, nothing is filtered out. Up to 2.5 bar, the evolution of S_2 is no longer proportional to S_1 but a plateau appears for a range of input intensities (between 1.5 and 2.5 arb. unit.). Three intensity regimes can be defined, labeled from I to III. In interval I, the incident intensity is too low and consequently SPM generation is not efficient enough to induce noise reduction. Interval II corresponds to the range of input intensities for which noise reduction is optimal. Although the input intensity S_1 increases by a factor 2, the spatially filtered output intensity S_2 remains stable. The fluctuations of S_1 versus S_2, $\frac{\delta S_1}{\delta S_2}$, rise up to 5 in this interval. Fundamental incident pairs of photons are efficiently converted in pairs of conjugated photons by FWM which results in a reduction of

#85217 - $15.00 USD Received 17 Jul 2007; revised 23 Aug 2007; accepted 29 Aug 2007; published 28 Sep 2007

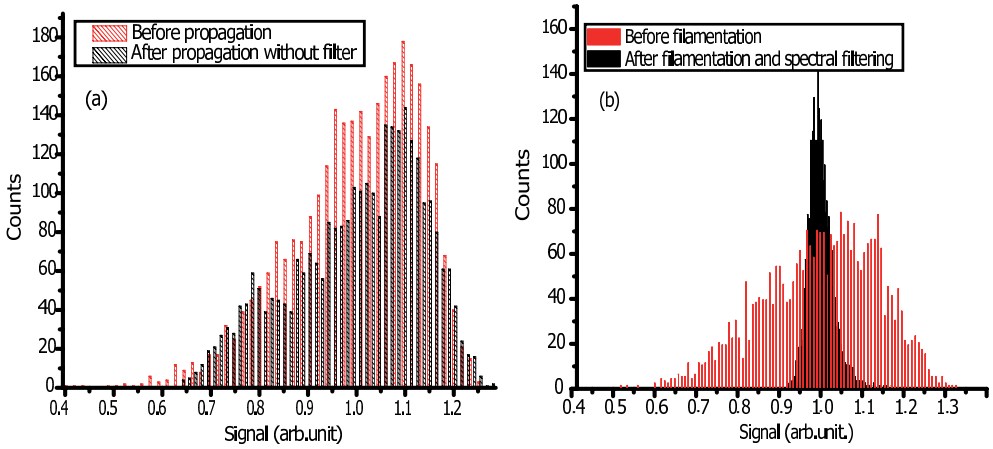

Fig. 10. Histograms of the fluctuations on the pulse intensities before (channel 1) and after (channel 2) propagation in a cell filled with 2 bar of argon gas. The average energy was set at 275 μJ. Statistic on 2000 laser shots. (a) Histogram made with no filtering applied. No noise reduction is observed. (b) The same experiment made with a [406 nm-414 nm] filter. An increase of 7 dB on the SNR is clearly visible on Channel 2.

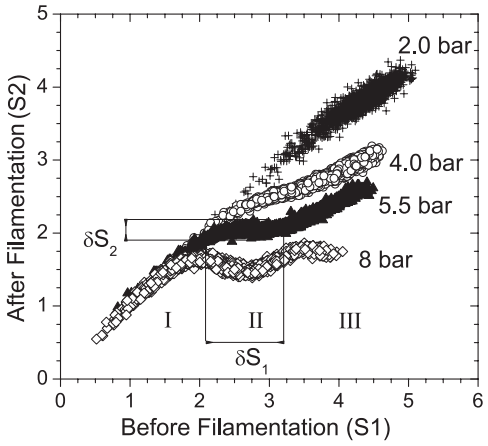

Fig. 11. Statistics on the intensities after propagation (S_2) for a large panel of input intensities (S_1) at several argon pressures. The average energy was set at 120 μJ. At low pressure (2 bar), an increase of the input intensity is correlated to a similar linear increase in the intensity after propagation. At higher pressure, the behavior can be divided in 3 intensity regions. In the low intensity case (region I), the power is too low to create many pairs of conjugated photon and induce a significant noise reduction on the input wavelengths. The intermediate input intensities case (region II) is the region where noise reduction is the highest. For a fluctuation δS_1 on the input intensity, a reduction of about 5 is observed on δS_2. In region III (high intensity cases), noise reduction is lost because cascaded events start to add wavelengths to the broadening.

#85217 - $15.00 USD Received 17 Jul 2007; revised 23 Aug 2007; accepted 29 Aug 2007; published 28 Sep 2007

the noise on the incident spectrum. In interval III, cascading processes take place which result in a further increase of the noise.

4. Conclusions

We investigated both experimentally and theoretically the filamentation process at 400 nm in Argon. The shape of the spectrum can be tailored with controllable parameters as initial chirp and cell pressure. Because of its highly nonlinear nature, filamentation is sensitive to the input energy noise which limits its use in closed-loop optimization algorithms available for pulse pulse shaping applications. We show in this paper that spectral filtering can be used to significantly reduce the fluctuation.

We propose, as further experiment, a two-steps 400 nm filaments generation. In a first low-pressurized Argon cell, a weak filament is generated and then, at the exit of the cell, the spectrum is filtered out in order to increase significantly the Signal-to-Noise Ratio. Then the chirp generated by the propagation through all the dispersive media (glass windows, lenses, Argon) and by the filamentation process itself has to be compensated with adapted chirped mirrors. This stage is necessary for increasing the peak power of the pulse before the second filamentation stage. In a second quite high-pressurized Argon cell, a long filament is created in order to broaden the spectrum as much as possible. Finally, the chirp generated by the second propagation stage is compensated by another chirped mirror. The performance of this procedure is currently under study.

Acknowledgments

This work was supported by the Swiss National Science Foundation in the framework of the CIBA (Coherent Identification of Bacteria in Air). We gratefully acknowledge H. Zbinden, N. Gisin, L. Bonacina, P. Billaud (Université de Genève) and E. Salmon (University of Lyon 1) for very fruitful discussions. We also thank M. Moret for the realization of the argon cell and his computational support and M. Gilli for algorithmic advices.

#85217 - $15.00 USD Received 17 Jul 2007; revised 23 Aug 2007; accepted 29 Aug 2007; published 28 Sep 2007